

Article

Green Synthesis of ZnO Nanostructures Using *Pyrus pyrifolia*: Antimicrobial, Photocatalytic and Dielectric Properties

Zainal Abidin Ali ^{1,2,*}, Iqabiha Shudirman ³, Rosiyah Yahya ³ , Gopinath Venkatraman ^{4,5} ,
Abdurahman Hajinur Hirad ⁶  and Siddique Akber Ansari ⁷ 

¹ Pusat Asasi Sains, Universiti Malaya, Kuala Lumpur 50603, Malaysia

² Centre for Ionics Universiti Malaya (C.I.U.M), Department of Physics, Faculty of Science, Universiti Malaya, Kuala Lumpur 50603, Malaysia

³ Department of Chemistry, Universiti Malaya, Kuala Lumpur 50603, Malaysia

⁴ Universiti Malaya Centre for Proteomics Research, Universiti Malaya, Kuala Lumpur 50603, Malaysia

⁵ Department of Biochemistry, Saveetha Dental College, Saveetha Institute of Medical & Technical Sciences, Saveetha University, Chennai 600 077, India

⁶ Department of Botany and Microbiology, College of Science, King Saud University, P.O. Box 2455, Riyadh 11451, Saudi Arabia

⁷ Department of Pharmaceutical Chemistry, College of Pharmacy, King Saud University, P.O. Box 2454, Riyadh 11451, Saudi Arabia

* Correspondence: zaba_87@um.edu.my

Abstract: In this study, zinc oxide nanostructures (ZnO NS) were synthesized using *Pyrus pyrifolia* fruit extract. Biophysical characterization results confirmed that the synthesized materials are crystalline wurtzite ZnO structures. Field emission scanning electron microscopy (FESEM) revealed that the ZnO NS are cubical, and the sizes range 20–80 nm. Transmission electron microscopy (TEM) and XRD results revealed a crystal lattice spacing of 0.23 nm and (101) the crystalline plane on ZnO NS. UV-Visible spectrophotometer results showed an absorbance peak at 373 nm. The ZnO NS demonstrated significant antibacterial activity analyzed by metabolic activity analysis and disc diffusion assay against *Escherichia coli* and *Staphylococcus aureus*. FESEM analysis confirmed the bacterial membrane disruption and the release of cytoplasmic contents was studied by electron microscopy analysis. Further, ZnO NS achieved good photocatalytic activity of decolorizing 88% of methylene blue (MB) in 60 min. The dielectric constant and loss of ZnO were found to be 3.19 and 2.80 at 1 kHz, respectively. The research findings from this study could offer new insights for developing potential antibacterial and photocatalytic materials.

Keywords: antibacterial; zinc oxide nanoparticles; photocatalytic; methylene blue; *Pyrus pyrifolia*; dielectric



Citation: Ali, Z.A.; Shudirman, I.; Yahya, R.; Venkatraman, G.; Hirad, A.H.; Ansari, S.A. Green Synthesis of ZnO Nanostructures Using *Pyrus pyrifolia*: Antimicrobial, Photocatalytic and Dielectric Properties. *Crystals* **2022**, *12*, 1808. <https://doi.org/10.3390/cryst12121808>

Academic Editors:

Yamin Leprince-Wang,

Guangyin Jing and Basma El Zein

Received: 27 September 2022

Accepted: 14 November 2022

Published: 12 December 2022

Publisher's Note: MDPI stays neutral with regard to jurisdictional claims in published maps and institutional affiliations.



Copyright: © 2022 by the authors. Licensee MDPI, Basel, Switzerland. This article is an open access article distributed under the terms and conditions of the Creative Commons Attribution (CC BY) license (<https://creativecommons.org/licenses/by/4.0/>).

1. Introduction

Nanotechnology involves the application of materials in the range of 1–100 nm. The applications span from coatings [1], gas sensing devices [2], solar cells [3], batteries [4], environmental catalysts and antimicrobials [5,6]. Metal and metal oxide nanomaterials have improved the efficiency and performance of such devices. Consequently, researchers have given ZnO much attention due to its biocompatibility, low cost, high photocatalytic efficiency and antimicrobial potential. Indeed, it is recognized as a multifunctional material, as it has played a significant role in various fields such as biomedical (e.g., antimicrobials anticancer, tissue engineering) [7–9], cosmetics industries [10] and photocatalysts [11]. ZnO nanostructures are II–VI semiconductors with a wide bandgap energy of 3.3 eV and a high excitation binding energy of 60 meV. Thus, the materials are suitable for large electrical fields, high temperatures and high-power functionalities such as photovoltaic cells and chemical sensors. ZnO nanocrystals mostly show a wurtzite structure with lattice parameters of $a = 0.325$ nm and $c = 0.520$ nm [12]. The scarcity of clean water has been a serious issue debated globally. Water contamination is severely inflicted everywhere.

This is due to the irresponsible and uncontrolled development of industries that release chemicals into streams [13]. For example, textile industries have used large amounts of dyes and water in their textile coloring process. The release of dye wastewater from this process substantially pollutes the aqueous environment, which was predicted to be 15–20% of the total industrial pollution [14]. The introduction of carcinogenic dye pollutants to the environment cause lethal side effects to human and aquatic organisms [15]. Therefore, finding ways to remove wastewater dyes before discharging them into the environment is necessary.

In recent years, ZnO has been intensively researched as a potential material to treat dye effluents. In this process, ZnO absorbs UV light with a wavelength equal to or less than 385 nm to generate radicals that, in turn, degrade the dyes. Recent studies demonstrated that the photodegradation of methylene blue (MB) was up to 98.3% [16]. Factors such as morphology [17], shape, size and concentrations of the ZnO can directly affect the efficiency of the photocatalytic activities [18]. For instance, Barnes et al. reported that lowering the concentration of ZnO from 1 to 0.1 g/L reduced the photodegradation performance from 18 to 7% [19]. Recognizing the simplicity and wide potential of ZnO as a photocatalytic agent, numerous approaches are being used to synthesize ZnO nanostructures. However, green synthesis is more advantageous than the conventional approach and hazardous chemical-free procedures [20,21] because it is eco-friendly. This technique is similar to chemical reduction, except that the extracts of natural products replace the reducing and stabilizing agent. Furthermore, studies have shown that the nature of biological elements and the concentrations of extracts could influence the size, shape, and optical properties of nanostructures [22–25].

ZnO is also gaining interest due to its electronic polarizability. This allows ZnO to be researched as a dielectric material. Dielectric materials are mainly applied in developing flexible electronic devices [26]. In addition, the dielectric properties of the developed material strongly depend on the synthesis conditions [27]. Lanje et al. reported that the ZnO obtained via the precipitation method has a dielectric constant of 14.52 at 100 kHz [28]. On the other hand, ZnO synthesized using starch as a stabilizing agent reported a dielectric constant in the range of 4–5 at the same frequency [27]. At the same time, numerous research studies have investigated the phytosynthesis of ZnO, but very few have discussed its dielectric or electrical properties. In the present work, we develop a facile method for the synthesis of ZnO nanostructures by using a fruit extract of *Pyrus pyrifolia*. To the best of our knowledge, this is the first study of ZnO NS synthesis using *P. pyrifolia* fruits. To study the interaction between ZnO nanostructures and the bacteria and the decolorization ability of MB, we studied antimicrobial assays and the photocatalytic reaction. Notably, the dielectric properties of ZnO NS have also been reported in this study.

2. Materials and Methods

2.1. Chemicals and Reagents

All chemicals used in this study were of analytical grade and used without further purification. The zinc nitrate ($\text{Zn}(\text{NO}_3)_2 \cdot 6\text{H}_2\text{O}$), Ethidium bromide (EB) and MB were purchased from Sigma Aldrich (Burlington, MA, USA). Acridine orange (AO) was obtained from VWR AMRESCO Life science, Radnor, PA, USA. Distilled water (DW) was used in all experiments.

2.2. Preparation of Extracts

Fresh fruits of *Pyrus pyrifolia* were obtained from a supermarket in Kuala Lumpur, Malaysia. The fruits were washed twice with DW to remove any dust and impurities, then 100 g of the fruit was cut into small pieces and ground with 100 mL DW. The resulting saturated extract was filtered through the Buchner funnel by vacuum filtration and further filtration procedures were carried out (e.g., using gravity filtration) to ensure a clear extract was attained.

2.3. Synthesis of ZnO Nanostructures

For the synthesis of ZnO nanostructures, 0.1 M $\text{Zn}(\text{NO}_3)_2 \cdot 6\text{H}_2\text{O}$ was prepared by dissolving 7.43 g of zinc nitrate in 250 mL DW and sonicated for 30 min to achieve complete dissolution. Aqueous fruit extract in the amount of 50 mL was introduced into the above solution, magnetically stirred for 15 min and left at room temperature for 24 h. Afterwards, the reaction solution was heated at 80 °C till the volume was reduced to 3/4 of its original volume and the color changed to a deep yellow paste [29]. Next, the paste was collected in a clean crucible and calcined at 450 °C for 60 min using a small benchtop muffle furnace (Barnstead/ThermoLyne furnace 1400, Thermo Scientific, Waltham, MA, USA). The calcined materials were washed with DW and ethanol to remove the impurities. Finally, the resultant materials were dried for 12 h in a vacuum oven at 70 °C to obtain the white zinc oxide powder.

2.4. Characterization of the ZnO

X-ray diffraction (XRD) analysis was performed using Ultima IV (Rigaku, Tokyo, Japan) at a scan speed of 2° min^{-1} and a wavelength of 1.5406 Å in the 2θ range of 20–90 degrees. The crystallite size of the resultant ZnO NS was calculated using the Scherrer Equation (1).

$$D = \frac{\kappa\lambda}{\beta\cos\theta} \quad (1)$$

where D is the average crystallite size (in Å), κ is the shape factor, λ is the X-ray wavelength of X-ray (1.5406 Å) Cu- $K\alpha$ radiation, β is the full width at half maximum (FWHM) of the diffraction peak and θ is the Bragg angle [30].

The UV-Vis absorbance spectra were obtained using a UV-1700 Spectrometer (Shimadzu, Kyoto, Japan) with measurements in the wavelength range of 300–500 nm. Fourier transform infrared (FT-IR) spectroscopy analysis was carried out to detect the possible functional groups involved in the synthesis of ZnO nanostructures. A PerkinElmer, Waltham, MA, USA, Frontier FT-IR Spectrophotometer in the attenuated total reflectance (ATR) mode in the range of 4000–500 cm^{-1} was used. Raman spectra were recorded in the backscattering geometry using a 632 nm HeNe laser with a LabRAM HR Evolution spectrometer, Kyoto, Japan. The morphological properties were characterized using FESEM (JEOL JSM 6701-F, Peabody, MA, USA) equipped with EDX analysis. EDX tests were carried out to identify the element and obtain the weight/atomic ratio of each element in the synthesized nanomaterials. Transmission electron microscopy (TEM) analysis was carried out on a (JEOL 2010, Peabody, MA, USA) instrument operated at an accelerating voltage of 200 kV. The Brunauer-Emmett-Teller (BET) nitrogen adsorption-desorption (Nova 2000E) was used to calculate the specific surface areas using desorption data. The sample was prepared using 200 mg of ZnO NS, which was subsequently degassed at 200 °C for 2 h to remove the moisture. Nitrogen gas was introduced as an adsorbent into the sample cell and the pressure changes due to the adsorption process were monitored via pressure transducers. When the saturation pressure was achieved, the sample was removed from the nitrogen atmosphere and heated to release the adsorbed nitrogen, which was then quantified.

2.5. Dielectric Studies

The dielectric studies of ZnO NS were carried out using a chemical impedance analyzer (Model: Hioki Im3590, Nagano, Japan). The as-synthesized ZnO nanostructure was compressed into pellets 13 mm in diameter and 0.539 mm in thickness by applying a force of 10 tons with a hydraulic press. The dielectric constant and loss were measured in the frequency range of 1 Hz–100 kHz.

2.6. Photocatalytic Decolorization of Methylene Blue

We placed 2.5 mg/L MB dye (50 mL) and 10 mg catalyst ZnO NS in a glass beaker and the suspension was magnetically stirred for 30 min in the dark to reach equilibrated adsorption between the ZnO NS and MB. Then the suspension was irradiated under UV light sources (Philips, $\lambda = 365 \text{ nm}$, 6 W) with continuous stirring. Another beaker containing

the same concentration of MB dye without ZnO was prepared as a control and underwent the same treatment as the one with ZnO. The samples (5 mL) were taken out at regular intervals of 0, 15, 30, 45 and 60 min, centrifuged for 5 min at 4000 rpm and the absorbance was measured using UV-Vis spectroscopy. The decolorization efficiencies of the dyes were estimated from the following equation [31]:

$$\text{Decolorization(\%)} = \frac{A_0 - A_t}{A_0} \times 100 \quad (2)$$

where A_0 represents the absorbance of dye before illumination and A_t denotes the absorbance of the dye after a specific irradiation time.

2.7. Antimicrobial Assay of ZnO NS

2.7.1. Disc Diffusion Assay

The antibacterial activity of the ZnO NS was studied using disc diffusion assay. Briefly, Gram-positive bacteria *B. subtilis* (ATCC 23857) and Gram-negative bacteria *E. coli* (ATCC 25922) were used to perform the antimicrobial assays. The freshly grown bacterial single colonies were spread in the Mueller-Hinton agar plate. The different concentrations (100, 200, 300 and 400 $\mu\text{g/mL}$) of ZnO NS solution (20 μL) were impregnated on the paper disc (6 mm diameter) and labelled as 1, 2, 3 and 4. The disc in the center was loaded with 20 μL DW and served as a control. The plates were then incubated for 24 h at 37 $^\circ\text{C}$. The bacterial inhibition zones observed around the discs were measured and tabulated.

2.7.2. Resazurin Assay Based Minimum Inhibitory Concentration (MIC) Determination

The MICs of the ZnO NS were determined by a standard broth microdilution assay in a 96 well plate. Briefly, the concentration of overnight grown bacterial pathogens was adjusted to 1×10^5 CFU/mL. The ZnO NS (500 $\mu\text{g/mL}$) were serially diluted (2-fold) in 175 μL of MHB with 10 μL of selected bacterial inoculum. The wells containing only MHB and the MHB containing bacteria were negative and positive controls, respectively. Then, the plates were incubated for 24 h at 37 $^\circ\text{C}$. Next, the MIC was determined by visually observing the turbidity. The lowest concentration of ZnO NS treated bacteria wells without turbidity were considered as the MIC [32]. Meanwhile, another set of experimental wells were flooded with 10 μL of resazurin and incubated for 60 min. The sample wells turned from blue to pink, indicating bacterial viability, and the minimal dosage of ZnO NS treated wells remained blue, indicating MIC [33].

2.7.3. Analysis of Bacterial Morphological Changes

The morphological changes of bacteria caused by the ZnO NS were examined by scanning electron microscopy. Briefly, *P. aeruginosa* and *B. subtilis* were treated with ZnO NS and incubated at 37 $^\circ\text{C}$ for 2 h. Then the cells were washed with PBS, followed by glutaraldehyde fixation for 6 h. The samples were then washed with H_2O and dehydrated with increasing concentrations of ethanol and acetone. Lastly, the samples were processed for gold coating and viewed under a field emission scanning electron microscope (FESEM).

3. Results and Discussion

3.1. ZnO NS Synthesis and UV-Vis Spectrum

The phytochemical constituents in the *P. pyrifolia* fruit extract chelate with the metallic zinc ions (Zn^{2+}) and form yellow-colored zinc coordinated complex sediment in the reaction medium [34]. Then, the obtained Zn complex was decomposed by calcining it at 450 $^\circ\text{C}$ for 60 min to get the nanostructured zinc oxide materials. The schematic diagram of *P. pyrifolia* mediated ZnO NS synthesis is represented in (Figure 1a).

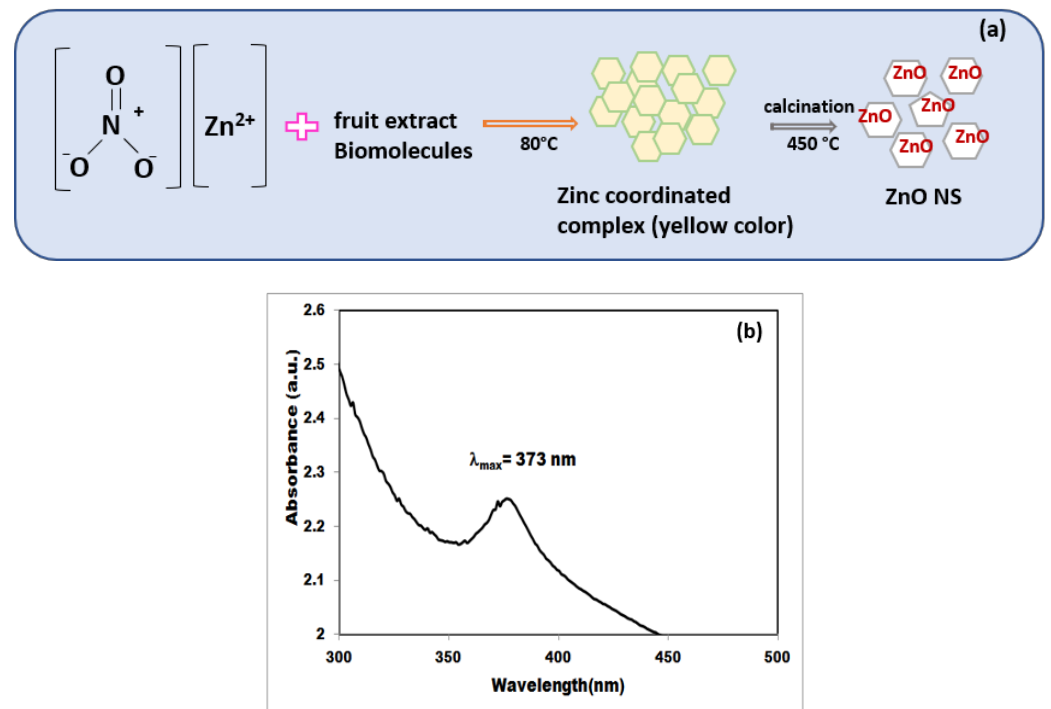


Figure 1. Schematic representation of zinc oxide nanostructures synthesis using *Pyrus pyrifolia* fruit extract (a). UV-Vis spectrum of the synthesized zinc oxide nanostructure solution (b).

Generally, UV-Vis spectral analysis is used to confirm the formation of metal and metal oxide nanoparticles. The synthesized aqueous ZnO NS solution showed that the synthesized nanoparticles exhibit an excitation wavelength of 373 nm (Figure 1b), which is almost similar to the range of results in the literature [11,22]. The band gap energy (E) of the synthesized ZnO nanostructure was estimated by applying the peak at 373 nm, using Equation (2).

$$E = \frac{hc}{\lambda_{max}} \quad (3)$$

where h is the Planck's constant and c is the speed of light in vacuum. E of the resultant ZnO NS was calculated to be 3.32 eV. This result is in accordance with the previous report on the synthesis of ZnO nanoparticles [35].

3.2. X-ray Diffraction Analysis of ZnO NS

The X-Ray diffraction peaks of the synthesized ZnO NS are shown in Figure 2. The X-ray diffraction patterns of the resultant ZnO NS showed different diffraction peaks at the 2θ values of 31.87° , 34.49° , 36.36° , 47.49° , 56.75° , 62.94° , 66.29° , 68.06° , 69.29° , 75.58° and 76.85° , which can be indexed to the (1 0 0), (0 0 2), (1 0 1), (1 0 2), (1 1 0), (1 0 3), (2 0 0), (1 1 2), (2 0 1), (0 0 4) and (2 0 2) planes, respectively. These observed diffraction peaks are highly matched with the hexagonal phase of the wurtzite ZnO structure (JCPDS card number: 36–1451). The sharp diffraction peaks demonstrate the high crystalline nature of the formation of ZnO particles. No obvious presence of unknown peaks implies a high purity of the synthesized ZnO NS. Our results are in accordance with an earlier report [36]. The crystallite size of the resultant ZnO NS was calculated using the diffraction peak of 36.36° and found to be 17 nm.

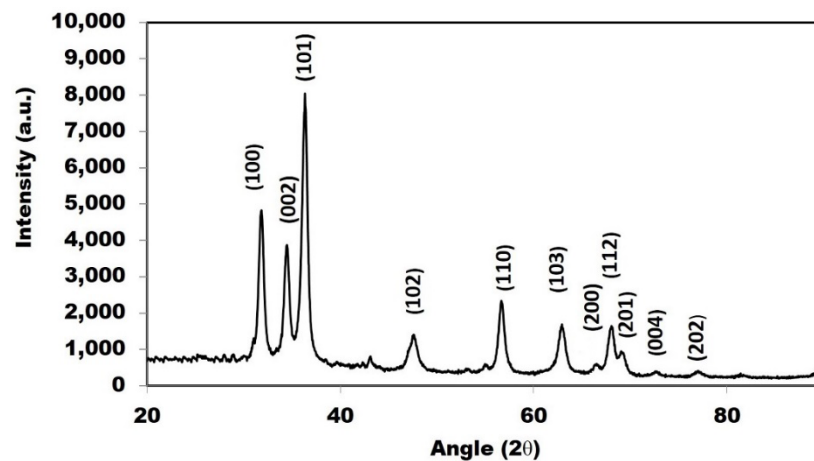


Figure 2. XRD pattern of the synthesized zinc oxide nanostructures.

3.3. FESEM and EDX Pattern of ZnO NS

The FESEM images showed that the diameters of the samples of ZnO nanostructures are in the range of 20–80 nm (Figure 3a,b). The ZnO is cubical, and the shape is almost uniform throughout the sample. The formation of clusters by the nanoparticles is mostly likely attributed to agglomeration, which is common in nano-sized materials. Furthermore, the elemental analysis spectrum results revealed the presence of zinc and oxygen in the densely populated nanoparticles region (Figure 3c). The elemental weight percentage is shown in the inset of (Figure 3c).

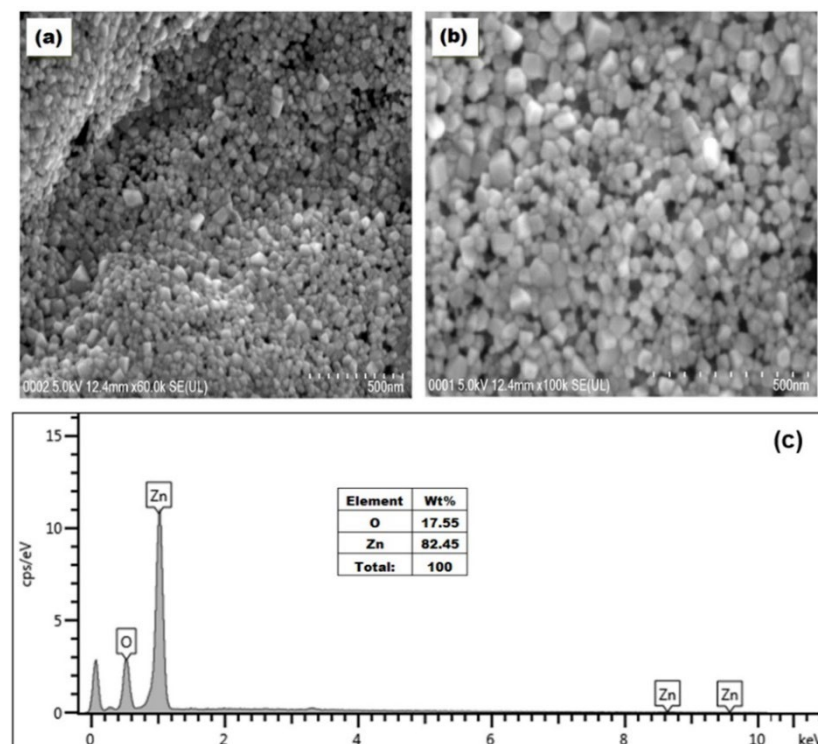


Figure 3. Scanning electron microscopic images of zinc oxide nanostructures at different magnifications (a,b). EDX pattern of zinc oxide nanostructures (c).

3.4. TEM and BET Measurement of Resultant Nanomaterials

To study the structure and morphology of the synthesized ZnO NS, the TEM analysis was employed, as shown in (Figure 4a), and thus the mean size of the particles can be analyzed. It is apparent from the TEM image that the shape of the ZnO particles is modified

from a spindle structure to a nearly spherical form due to the involvement of the extract in the crystallization process. This further asserts the findings of Bayrami et al. [37]. The results showed the lattice fringes spacing was measured to be 0.23 nm, which can be attributed to the space between two planes (101) of the wurtzite ZnO NS [38]. Moreover, this result corroborates the crystal lattice spacing determined from the above XRD peak 2θ value of 36.36° with a corresponding lattice plane of (101).

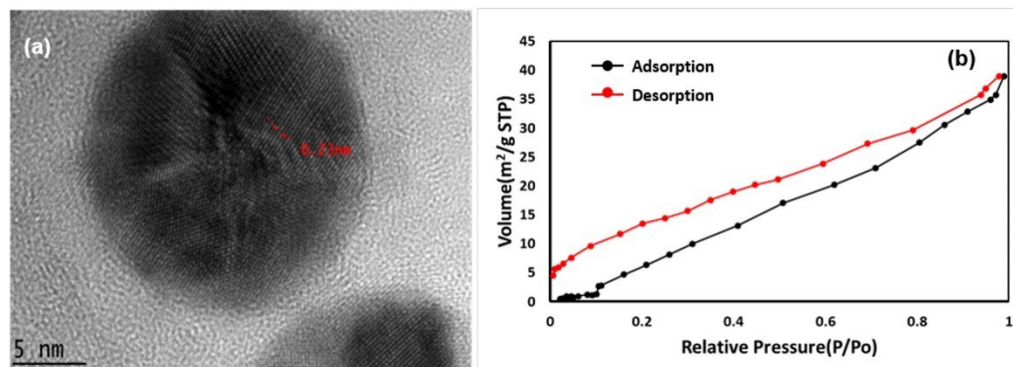


Figure 4. Transmission electron microscopy images of zinc oxide nanostructures (a), BET adsorption-desorption isotherms of resultant zinc oxide nanostructures (b).

To examine the surface properties of resultant ZnO NS, the Brunauer-Emmett-Teller (BET) nitrogen adsorption-desorption isotherms were measured, as shown in (Figure 4b). In both cases, it is evident that the volume of the sample increases monotonously with increasing relative pressure. Particularly, at low pressure (between 0 and 0.1 P/P_0), the adsorption can be largely attributed to its microporous filling. A nearly similar trend is noticed for desorption. However, with the enhancement in pressure, a gentle hysteresis loop ensues, which is a habitual hallmark of mesoporous materials [39]. The BET measurements estimate the surface area of ZnO to be $21.4 \text{ m}^2/\text{g}$. Furthermore, relating the ZnO NS surface area with their photocatalytic performances, two trends of results have been reported, as the photocatalytic activity of ZnO nanoparticles increased with both an increase in specific surface area [40] and a decrease in specific surface area [41]. Moreover, it has been reported that, although the ZnO NS have a larger surface area and it has no significant effect on the pore diameter, it may result in a larger active site [42]. The obtained data curve denotes typical type II isotherms, which relate to the nonporous characteristic of solids [37].

3.5. FTIR and Raman Measurement of ZnO NS

FTIR spectra of the *P. pyriformis* fruit extract and synthesized ZnO nanostructures before and after calcination were showed in (Figure 5a, A,B,C). A vibration band of fruit extract showed peaks at 3382 , 1638 , 1488 , 1381 and 845 cm^{-1} . The peak at 3382 cm^{-1} corresponds to the O-H stretching functional group [43]. The peaks at 1638 and 1488 cm^{-1} can be attributed to the carbonyl (C=O) functional group and bending vibration of the $\text{sp}^2 \text{ C}=\text{C}$ aromatic ring [44], respectively. The obtained peaks at 1381 and 845 cm^{-1} are probably due to the alkene group of C-H stretching and C-N amine [45], respectively. Phenolic contents in the extract of pear may also be involved in the formation of ZnO NS. Momeni et al. suggested that the peaks that range from 3500 to 3100 , 1720 , 1605 , 1395 and 1100 cm^{-1} can be linked to the free OH in the extract, thus forming hydrogen bonds, a carbonyl group (C=O), a stretching C=C aromatic ring and C-OH and C-H stretching vibrations. Correspondingly, these indicate the presence of phenolic structures in the plant extract [46]. The FTIR spectrum of synthesized zinc complex before calcination showed peaks at 3412 , 1635 and 1385 cm^{-1} . A comparison of FTIR spectra revealed a slight shift in the peaks of the extract and the zinc complex. This is anticipated due to the adsorption of the plant extract (C-H stretching vibration, O-H and carbonyl groups) onto the zinc surface, which may be involved in the synthesis of the nanoparticles. Further, the FTIR spectrum of the

ZnO NS revealed no significant peaks due to the decomposition of bioactive functional groups during calcination [5].

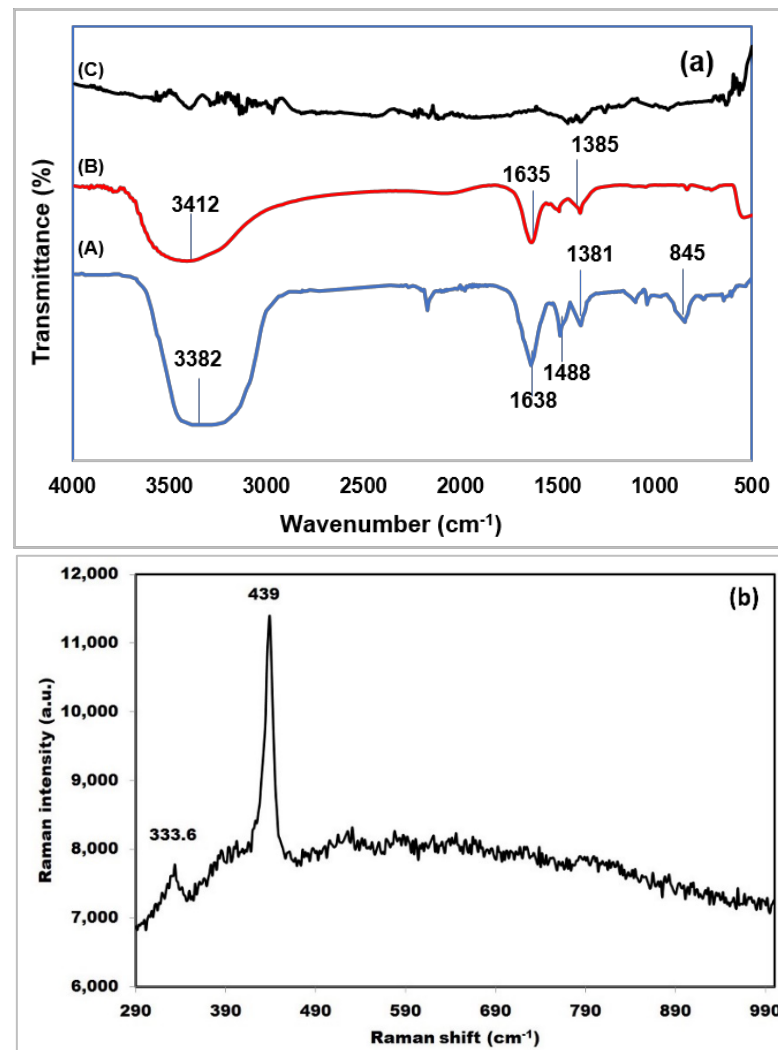


Figure 5. (a) FTIR spectrum of *P. pyrifolia* fruit extract (A), ZnO NS before calcination (B), calcined ZnO NS (C) and Raman spectrum of ZnO nanostructures (b).

The Raman spectrum of the ZnO nanostructures from 290 cm⁻¹ to 990 cm⁻¹ is shown in Figure 5b. The obtained spectrum has a Raman peak comparable to ZnO nanocrystals presented in an earlier report [47] with a slight shift (in the range of 1–2 cm⁻¹) caused by different crystal sizes [48]. Theoretically, the wurtzite crystal structure of ZnO belongs to the C6v4, possessing 2 formula units in each primitive cell with all the atoms lodging the C3V sites [49]. The major, sharp peak labelled as E2 at 439 cm⁻¹ is recognized as Raman active optical phonon mode, which is the characteristic of the wurtzite hexagonal phase ZnO. Raman modes at 333.6 and 439 cm⁻¹ are denoted as 2E2 and E2 modes, respectively [47,48].

3.6. ZnO NS Photocatalytic Decolorization of Methylene Blue

The photocatalytic decolorization efficiency of ZnO NS on MB was observed using different amounts of ZnO catalyst (1 mg, 5 mg, 10 mg and 20 mg) in 50 mL of 2.5 mg/L MB solution under UV light for 60 min. The decolorization was analyzed by measuring the absorbance peak of the MB. As shown in Figure 6a, a lower absorbance peak indicates that more MB is decolorized and vice-versa. These results showed that by using 10 mg of ZnO, the absorbance peak was the lowest compared to the other tested ZnO concentrations, inferring the highest amount of MB decolorized at this particular concentration. This may

be attributed to the increase of the catalyst concentration, which subsequently increases the production of ROS and accelerates the number of active sites on the ZnO NS for the reaction.

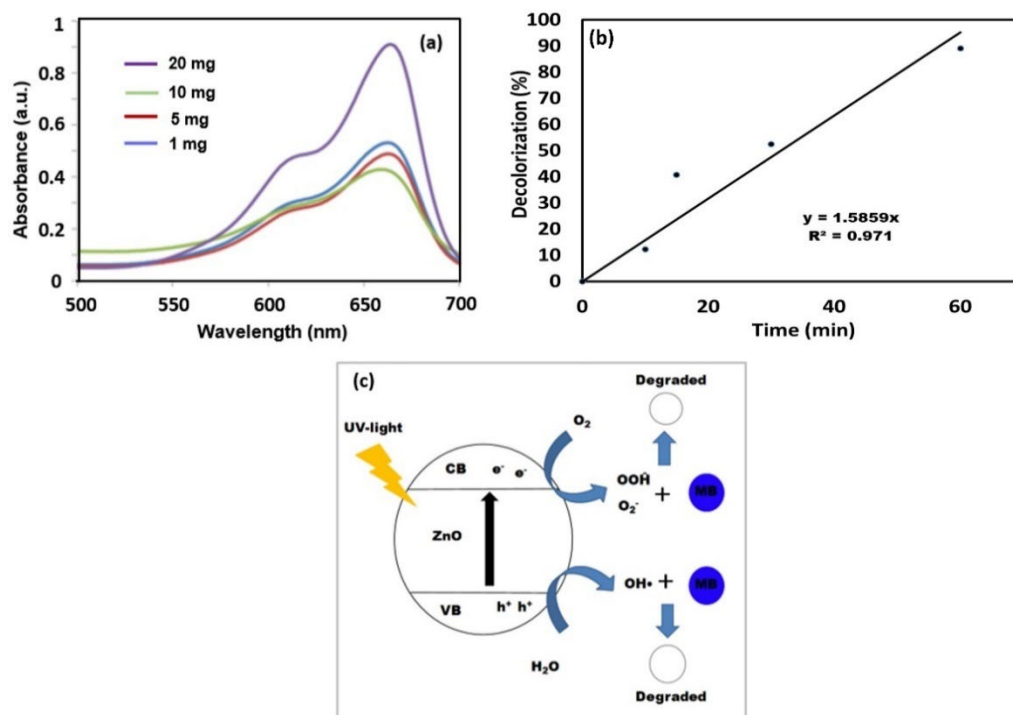


Figure 6. The absorption spectrum of photodegradation efficiency of MB (a), degradation percentage of MB (b) and schematic illustration of photodegradation of methylene blue by ZnO NS (c).

As seen in Figure 6b, the decolorization exhibits a linear behavior indicating that degradation is directly proportional to the amount of ZnO. However, it was also observed that when the catalyst loading was further increased to 20 mg, the absorbance peak of the MB was the highest, corresponding to the lowest decolorization of MB. The decrease in the photocatalytic decolorization efficiency is probably due to the agglomeration of the catalyst particles. As a result, the specific surface area decreased and subsequently decreased the number of active sites [50]. Moreover, a high quantity of ZnO NS would lower the opacity, turbidity of the suspension and light scattering of the catalyst particles. The more significant amount of nanoparticle suspension may have increased UV shading to hinder photocatalytic activity [19,51]. This would decrease the path of irradiation through the sample [52]. Therefore, in our case, the most effective decolorization for MB was recorded with 10 mg of ZnO NS catalyst.

Figure 6c represents the photocatalytic mechanism for MB in the presence of ZnO. Adsorption and adhesion of the MB dye molecules on the surface of ZnO result in the degradation of the MB. It has been extensively discussed that the photocatalytic decolorization of MB by semiconductors, such as ZnO, can occur due to hydroxyl radicals ($\bullet OH$) [53,54]. The $\bullet OH$ can be formed either from (i) the highly hydroxylated ZnO surface or (ii) by direct oxidation of dye pollutants under UV irradiation. Moreover, there is also a possibility that the $\bullet OH$ co-occurs by both methods. The photo decolorization process starts when ZnO absorbs UV light of energy equal to or higher than its bandgap (3.37 eV). This promotes the formation of free electrons (e^-) and holes (h^+) in the conduction and valence bands, respectively. These electrons can either recombine with the holes (and scatter the captivated energy as heat), or the electron-hole pairs can contribute to redox reactions. In the case of participating redox reactions, the electron-hole pairs can generate $\bullet OH$ either from the reaction of h^+ with water or with OH^- anions [50]. On the other hand, the response of dissolved O_2 and e^- will produce superoxide ($\bullet O_2^-$) and may also proceed to make OOH .

All of these active oxygen species ($\bullet\text{O}_2^-$) and free hydroxyl radicals ($\bullet\text{OH}$, $\bullet\text{OOH}$) could also be involved in the photodegradation of the MB [16].

3.7. Dielectric Studies

The dielectric constant is a measure of the capability of a material to stock electrical energy in an electric field. It is a ratio of the material permittivity to the free space permittivity. Permittivity (ϵ) is a measure of the ability of a material to be polarized by an electric field. An efficient dielectric material supports polarization with minimal dissipation or loss of energy. The dissipation of energy in the form of heat, as the movement of charges in an alternating electromagnetic field occurs, as polarization switches direction. This is known as the dielectric loss (D) or $\tan \delta$ (loss tangent). It is proportional to the amount of energy stored and dissipated due to the presence of an applied electric field. The dielectric constant and loss were assessed in the frequency range from 1 Hz to 100 kHz in the present study. The dielectric constant, also known as relative permittivity, is determined using the equation:

$$\epsilon_r = \frac{C \times d}{\epsilon_0 A}$$

where C is the capacitance of the sample, d and A are the thickness and the area of the sample pellet, respectively, and ϵ_0 is the dielectric permittivity of vacuum (8.854×10^{-12} F/m). The ϵ_r and $\tan \delta$ for the synthesized ZnO were found to be 3.19 and 2.80 at 1 kHz, respectively. A recent report of the synthesized ZnO NPs by the co-precipitation method demonstrated the value of the dielectric constant and loss to be approximately 12 and 0.01, respectively [55], while ZnO NPs synthesized using sol-gel observed the dielectric constant and loss to be 40 and 50, respectively [56]. Apart from the preparation conditions that can influence the value of the dielectric properties [27], it is noteworthy to mention that the compression force used in preparing the pellet must also be considered because different compression forces will result in different void spaces between the particles [57], and void space affects electrical measurements. Therefore, a direct comparison of the values is difficult, as many aspects and factors come into play. Figure 7a,b represents the deviation of the dielectric constant (ϵ) and dielectric loss ($\tan \delta$) with respect to frequency at room temperature (300 K). The values of ϵ_r and D were found to decline with increasing frequency. The decrement rate was observed to be quicker at a lower frequency and slower at a higher frequency. The decrease of the dielectric constant at high frequencies is typical because any species contributing to polarization will have their space charges reduced under the applied field at higher frequencies [58]. Polarization could arise from electronic dislodgment, ionic displacement, dipole orientation and space charge displacement [56].

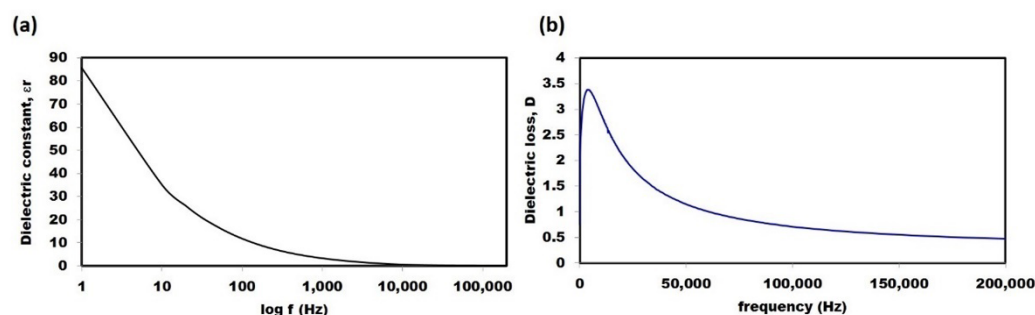


Figure 7. Electrical properties of ZnO NS; (a) dielectric constant and (b) dielectric loss.

3.8. Antibacterial Activity of ZnO NS

3.8.1. MIC Determination and Metabolic Activity

Although industrial effluents pollute the environment, the emergence of pathogenic bacterial drug resistance epitomizes the high risk to public health. Nanomaterials are considered alternate antimicrobials due to their unique physiochemical properties. To determine the MIC level of ZnO NS against *P. aeruginosa* and *B. subtilis*, a broth microdi-

lution assay was performed. The turbidity observation results showed that the ZnO NS significantly inhibited the growth of *P. aeruginosa* and *B. subtilis* with MIC values of 125 and 250 $\mu\text{g}/\text{mL}$ (Figure 8, Row B and D), respectively. A similar pattern of greater and lesser antibacterial activity was observed against *P. aeruginosa* and *B. subtilis*, which may be due to the differential cell wall structure of Gram-positive and Gram-negative bacteria [59]. ZnO NPs demonstrated a prominent antibacterial effect; their combinations are used in food additives due to their non-toxic nature to humans within FDA approved concentrations [60]. The turbid white color appearance of increasing ZnO NS concentrations slightly interfered with the determination of MIC and whether bacterial growth caused the turbidity. Furthermore, the samples that were incubated with resazurin after 60 min showed that the metabolically active bacterial cells appeared to change colors, from blue (resazurin) to pink (resorufin), as shown in Figure 8 (Row A and C). The lowest dosage of ZnO NS (125 and 250 $\mu\text{g}/\text{mL}$) exposed *P. aeruginosa* and *B. subtilis*, remaining unchanged in its blue color, were determined as MIC. Moreover, these results are in line with the MIC of turbidity observation analysis.

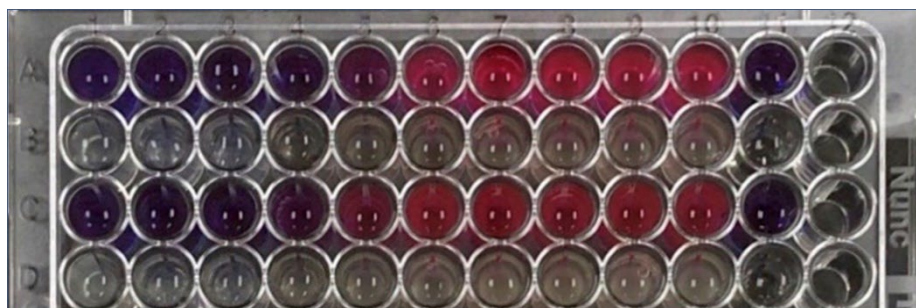


Figure 8. Antibacterial activity resazurin assay (A,C) and turbidity observation (B,D) of ZnO NS against *P. aeruginosa* and *B. subtilis*, respectively.

3.8.2. Disc Diffusion Assay

The antibacterial activity of ZnO NS was studied against *B. subtilis* and *P. aeruginosa* by disc diffusion assay. The assay results showed clear growth inhibition on the plates against both the tested bacteria (Figure 9a,d). From the results, the DW loaded control disc in the center, and for lesser concentrations of ZnO NS impregnated discs (1. 100 $\mu\text{g}/\text{mL}$ and 2. 200 $\mu\text{g}/\text{mL}$), did not show any inhibition against both the tested bacteria. In contrast, a clear zone of inhibition was observed at increasing concentrations of ZnO NS discs (3. 300 $\mu\text{g}/\text{mL}$ and 4. 400 $\mu\text{g}/\text{mL}$). A higher inhibitory zone was observed at 8 mm for both bacteria at a 400 $\mu\text{g}/\text{mL}$ dosage of ZnO NS. These results showed an increased bacterial inhibitory effect as ZnONS dosage was increased, which was correlated with an earlier report [61].

To study the ZnO NS effect on bacterial cells, the ZnO NS treated cells were imaged and compared with the control bacteria. Figure 9b,e shows the bacteria without any treatment, which demonstrated a rod-like shape with a smooth cell membrane surface. After 2 h ZnO NS treatment, our observations show that both bacteria underwent structural changes, including membrane damage, pits and holes on the cell membranes (Figure 9c,f). Furthermore, the leakage of cytoplasmic content was observed, which led to bacterial death. The bactericidal effect of ZnO is ascribed to multiple reasons, such as cell wall and cell membrane damage and the release of zinc ions and their ability to produce ROS, which causes oxidative stress to the bacteria [62]. It was reported that the release of Zn^{2+} ions accelerates the ROS generation in the bacterial surface and may involve oxidizing glutathione and induce lipid peroxidation, which subsequently causes bacterial lysis [63].

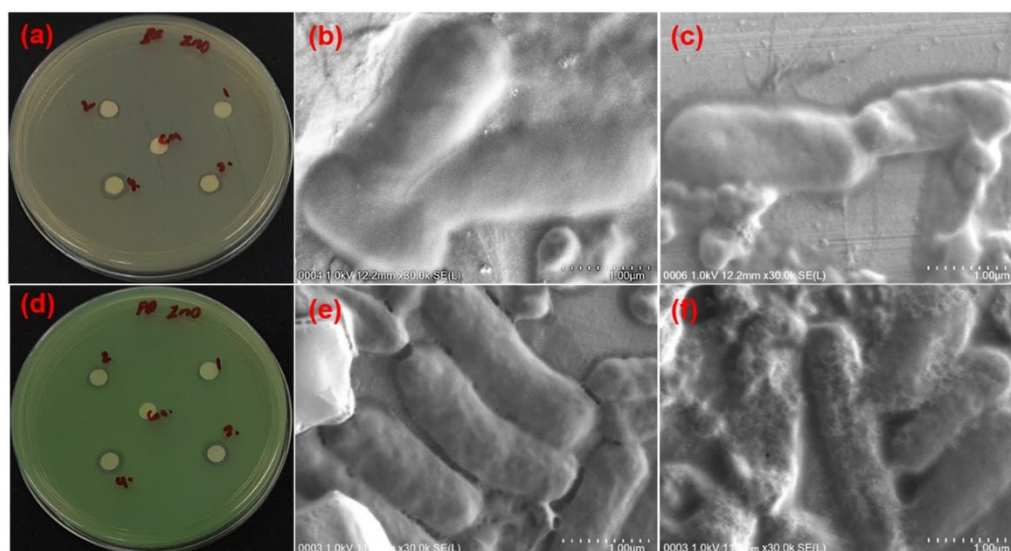


Figure 9. Antibacterial disc diffusion assay of ZnO NS against *B. subtilis* and *P. aeruginosa* (a,d). Discs 1, 2, 3, 4 and control were loaded with 20 μ L of ZnO NS (100, 200, 300, 400 μ g/mL) and DW. FESEM image of bacterial control (b,e) and after ZnO NS treatment (c,f).

4. Conclusions

ZnO nanostructures were successfully synthesized using *Pyrus pyrifolia* fruit extract as a reducing agent by the green synthesis route. The structural, morphological and optical properties of the ZnO nanostructures were analyzed by FESEM, UV-Vis, FTIR and Raman. The XRD pattern result confirmed the wurtzite structure of ZnO nanostructures. FESEM analysis revealed the average size of ZnO NS in the range of 20–80 nm. Flavonoids/limonoids/carotenoids, proteins and other functional groups in the fruit extract are likely responsible for forming ZnO nanostructures. Further, the ZnO NS demonstrated significant antibacterial activity against *B. subtilis*, and *P. aeruginosa*, which was confirmed by metabolic assay and morphological analysis. MB dye was effectively decolorized under UV light by controlling the concentration and catalyst loading of the MB. The synthesized ZnO NS exhibits a typical pattern of dielectric constant and loss of ZnO with respect to the frequency. The results of this study may provide new insights into the utilization of green-synthesized ZnO NS for developing novel antimicrobial combinations to treat bacterial infections, and for environmental photocatalysts to remove pollutant antibiotics.

Author Contributions: Conceptualization, investigation and writing original draft preparation, Z.A.A.; validation, R.Y.; formal analysis, I.S.; data curation, A.H.H.; writing, review and editing, G.V.; project administration, S.A.A. All authors have read and agreed to the published version of the manuscript.

Funding: The research was supported by RU Geran Fakulti Program (GPF040A-2020) from the University of Malaya, Malaysia. The authors also thank the Deanship of Scientific Research at King Saud University for funding this work through research group No (RG-1441-362).

Institutional Review Board Statement: Not applicable.

Informed Consent Statement: Not applicable.

Data Availability Statement: Not applicable.

Acknowledgments: The authors extend their appreciation to the Deanship of Scientific Research at King Saud University for funding this work through research group No RG-1441-362.

Conflicts of Interest: The authors declare no conflict of interest.

References

1. Asmatulu, R.; Claus, R.; Mecham, J.; Corcoran, S. Nanotechnology-associated coatings for aircrafts. *Mater. Sci.* **2007**, *43*, 415–422. [[CrossRef](#)]
2. Kalantar-zadeh, K.; Fry, B. *Nanotechnology-Enabled Sensors*; Springer Science & Business Media: Berlin/Heidelberg, Germany, 2007.
3. Im, J.-H.; Jang, I.-H.; Pellet, N.; Grätzel, M.; Park, N.-G. Growth of $\text{CH}_3\text{NH}_3\text{PbI}_3$ cuboids with controlled size for high-efficiency perovskite solar cells. *Nat. Nanotechnol.* **2014**, *9*, 927–932. [[CrossRef](#)] [[PubMed](#)]
4. Lee, S.W.; Yabuuchi, N.; Gallant, B.M.; Chen, S.; Kim, B.-S.; Hammond, P.T.; Shao-Horn, Y. High-power lithium batteries from functionalized carbon-nanotube electrodes. *Nat. Nanotechnol.* **2010**, *5*, 531. [[CrossRef](#)] [[PubMed](#)]
5. Sakthi Mohan, P.; Sonsuddin, F.; Mainal, A.B.; Yahya, R.; Venkatraman, G.; Vadivelu, J.; Al-Farraj, D.A.; Al-Mohaimed, A.M.; Alarjani, K.M. Facile In-Situ Fabrication of a Ternary ZnO/TiO₂/Ag Nanocomposite for Enhanced Bactericidal and Biocompatibility Properties. *Antibiotics* **2021**, *10*, 86. [[CrossRef](#)] [[PubMed](#)]
6. Gopinath, V.; MubarakAli, D.; Vadivelu, J.; Manjunath Kamath, S.; Syed, A.; Elgorban, A.M. Synthesis of biocompatible chitosan decorated silver nanoparticles biocomposites for enhanced antimicrobial and anticancer property. *Process Biochem.* **2020**, *99*, 348–356. [[CrossRef](#)]
7. Mani, V.M.; Nivetha, S.; Sabarathinam, S.; Barath, S.; Das, M.P.A.; Basha, S.; Elfasakhany, A.; Pugazhendhi, A. Multifunctionalities of mycosynthesized zinc oxide nanoparticles (ZnONPs) from *Cladosporium tenuissimum* FCBG: Antimicrobial additives for paints coating, functionalized fabrics and biomedical properties. *Prog. Org. Coat.* **2022**, *163*, 106650. [[CrossRef](#)]
8. Gopinath, V.; Kamath, S.M.; Priyadarshini, S.; Chik, Z.; Alarfaj, A.A.; Hirad, A.H. Multifunctional applications of natural polysaccharide starch and cellulose: An update on recent advances. *Biomed. Pharmacother.* **2022**, *146*, 112492. [[CrossRef](#)]
9. Prasad, K.S.; Prasad, S.K.; Veerapur, R.; Lamraoui, G.; Prasad, A.; Prasad, M.N.N.; Singh, S.K.; Marraiki, N.; Syed, A.; Shivamallu, C. Antitumor Potential of Green Synthesized ZnONPs Using Root Extract of *Withania somnifera* against Human Breast Cancer Cell Line. *Separations* **2021**, *8*, 8. [[CrossRef](#)]
10. Lu, P.-J.; Huang, S.-C.; Chen, Y.-P.; Chiueh, L.-C.; Shih, D.Y.-C. Analysis of titanium dioxide and zinc oxide nanoparticles in cosmetics. *J. Food Drug Anal.* **2015**, *23*, 587–594. [[CrossRef](#)]
11. Suresh, D.; Nethravathi, P.C.; Udayabhanu; Rajanaika, H.; Nagabhushana, H.; Sharma, S.C. Green synthesis of multifunctional zinc oxide (ZnO) nanoparticles using *Cassia fistula* plant extract and their photodegradative, antioxidant and antibacterial activities. *Mater. Sci. Semicond. Process.* **2015**, *31*, 446–454. [[CrossRef](#)]
12. Özgür, Ü.; Alivov, Y.I.; Liu, C.; Teke, A.; Reshchikov, M.; Doğan, S.; Avrutin, V.; Cho, S.-J.; Morkoc, H. A comprehensive review of ZnO materials and devices. *J. Appl. Phys.* **2005**, *98*, 11. [[CrossRef](#)]
13. Fanun, M. *The Role of Colloidal Systems in Environmental Protection*; Elsevier: Amsterdam, The Netherlands, 2014.
14. Foroutan, R.; Peighambaroust, S.J.; Boffito, D.C.; Ramavandi, B. Sono-Photocatalytic Activity of Cloisite 30B/ZnO/Ag₂O Nanocomposite for the Simultaneous Degradation of Crystal Violet and Methylene Blue Dyes in Aqueous Media. *Nanomaterials* **2022**, *12*, 3103. [[CrossRef](#)]
15. Wei, X.; Chen, D.; Wang, L.; Ma, Y.; Yang, W. Carboxylate-functionalized hollow polymer particles modified polyurethane foam for facile and selective removal of cationic dye. *Appl. Surf. Sci.* **2022**, *579*, 152153. [[CrossRef](#)]
16. Siripireddy, B.; Mandal, B.K. Facile green synthesis of zinc oxide nanoparticles by *Eucalyptus globulus* and their photocatalytic and antioxidant activity. *Adv. Powder Technol.* **2017**, *28*, 785–797. [[CrossRef](#)]
17. Marquez, J.R.; Rodríguez, C.M.B.; Herrera, C.M.; Rosas, E.R.; Angel, O.Z.; Pozos, O.T. Effect of surface morphology of ZnO electrodeposited on photocatalytic oxidation of methylene blue dye part I: Analytical study. *Int. J. Electrochem. Sci.* **2011**, *6*, 4059–4069.
18. McLaren, A.; Valdes-Solis, T.; Li, G.; Tsang, S.C. Shape and size effects of ZnO nanocrystals on photocatalytic activity. *J. Am. Chem. Soc.* **2009**, *131*, 12540–12541. [[CrossRef](#)]
19. Barnes, R.J.; Molina, R.; Xu, J.; Dobson, P.J.; Thompson, I.P. Comparison of TiO₂ and ZnO nanoparticles for photocatalytic degradation of methylene blue and the correlated inactivation of gram-positive and gram-negative bacteria. *J. Nanopart. Res.* **2013**, *15*, 1432. [[CrossRef](#)]
20. Ramesh, M.; Anbuvaran, M.; Viruthagiri, G. Green synthesis of ZnO nanoparticles using *Solanum nigrum* leaf extract and their antibacterial activity. *Spectrochim. Acta Part A Mol. Biomol. Spectrosc.* **2015**, *136*, 864–870. [[CrossRef](#)]
21. Suresh, D.; Shobharani, R.; Nethravathi, P.; Kumar, M.P.; Nagabhushana, H.; Sharma, S. *Artocarpus gomezianus* aided green synthesis of ZnO nanoparticles: Luminescence, photocatalytic and antioxidant properties. *Spectrochim. Acta Part A Mol. Biomol. Spectrosc.* **2015**, *141*, 128–134. [[CrossRef](#)]
22. Sangeetha, G.; Rajeshwari, S.; Venckatesh, R. Green synthesis of zinc oxide nanoparticles by *aloe barbadensis miller* leaf extract: Structure and optical properties. *Mater. Res. Bull.* **2011**, *46*, 2560–2566. [[CrossRef](#)]
23. Philip, D. Green synthesis of gold and silver nanoparticles using *Hibiscus rosa sinensis*. *Phys. E Low-Dimens. Syst. Nanostruct.* **2010**, *42*, 1417–1424. [[CrossRef](#)]
24. Kora, A.J.; Sashidhar, R.; Arunachalam, J. Gum kondagogu (*Cochlospermum gossypium*): A template for the green synthesis and stabilization of silver nanoparticles with antibacterial application. *Carbohydr. Polym.* **2010**, *82*, 670–679. [[CrossRef](#)]
25. Kumar, V.; Yadav, S.K. Plant-mediated synthesis of silver and gold nanoparticles and their applications. *J. Chem. Technol. Biotechnol.* **2009**, *84*, 151–157. [[CrossRef](#)]

26. Chittibabu, S.K.; Chintagumpala, K.; Chandrasekhar, A. Porous dielectric materials based wearable capacitance pressure sensors for vital signs monitoring: A review. *Mater. Sci. Semicond. Process.* **2022**, *151*, 106976. [[CrossRef](#)]
27. Zamiri, R.; Singh, B.; Belsley, M.S.; Ferreira, J. Structural and dielectric properties of Al-doped ZnO nanostructures. *Ceram. Int.* **2014**, *40*, 6031–6036. [[CrossRef](#)]
28. Lanje, A.S.; Sharma, S.J.; Ningthoujam, R.S.; Ahn, J.-S.; Pode, R.B. Low temperature dielectric studies of zinc oxide (ZnO) nanoparticles prepared by precipitation method. *Adv. Powder Technol.* **2013**, *24*, 331–335. [[CrossRef](#)]
29. Jayachandran, A.; Aswathy, T.R.; Nair, A.S. Green synthesis and characterization of zinc oxide nanoparticles using Cayratia pedata leaf extract. *Biochem. Biophys. Rep.* **2021**, *26*, 100995. [[CrossRef](#)]
30. Cullity, B.D. *Elements of X-ray Diffraction*; Addison-Wesley Publishing: Boston, MA, USA, 1956.
31. Karnan, T.; Selvakumar, S.A.S. Biosynthesis of ZnO nanoparticles using rambutan (*Nephelium lappaceum* L.) peel extract and their photocatalytic activity on methyl orange dye. *J. Mol. Struct.* **2016**, *1125*, 358–365. [[CrossRef](#)]
32. Khan, M.S.; Ranjani, S.; Hemalatha, S. Synthesis and characterization of Kappaphycus alvarezii derived silver nanoparticles and determination of antibacterial activity. *Mater. Chem. Phys.* **2022**, *282*, 125985. [[CrossRef](#)]
33. Chakansin, C.; Yostaworakul, J.; Warin, C.; Kulthong, K.; Boonrungsiman, S. Resazurin rapid screening for antibacterial activities of organic and inorganic nanoparticles: Potential, limitations and precautions. *Anal. Biochem.* **2022**, *637*, 114449. [[CrossRef](#)]
34. Selvanathan, V.; Aminuzzaman, M.; Tan, L.X.; Win, Y.F.; Cheah, E.S.G.; Heng, M.H.; Tey, L.-H.; Arullappan, S.; Algethami, N.; Alharthi, S.S.; et al. Synthesis, characterization, and preliminary in vitro antibacterial evaluation of ZnO nanoparticles derived from soursop (*Annona muricata* L.) leaf extract as a green reducing agent. *J. Mater. Res. Technol.* **2022**, *20*, 2931–2941. [[CrossRef](#)]
35. Sadiq, H.; Sher, F.; Sehar, S.; Lima, E.C.; Zhang, S.; Iqbal, H.M.N.; Zafar, F.; Nuhanović, M. Green synthesis of ZnO nanoparticles from Syzygium Cumini leaves extract with robust photocatalysis applications. *J. Mol. Liq.* **2021**, *335*, 116567. [[CrossRef](#)]
36. Vijayakumar, S.; Vaseeharan, B.; Malaikozhundan, B.; Shobiya, M. Laurus nobilis leaf extract mediated green synthesis of ZnO nanoparticles: Characterization and biomedical applications. *Biomed. Pharmacother.* **2016**, *84*, 1213–1222. [[CrossRef](#)]
37. Bayrami, A.; Alioghli, S.; Rahim Pouran, S.; Habibi-Yangjeh, A.; Khataee, A.; Ramesh, S. A facile ultrasonic-aided biosynthesis of ZnO nanoparticles using *Vaccinium arctostaphylos* L. leaf extract and its antidiabetic, antibacterial, and oxidative activity evaluation. *Ultrason. Sonochem.* **2019**, *55*, 57–66. [[CrossRef](#)]
38. Zhou, R.; Wu, X.-Y.; Zhao, Q.; Liu, K.-K.; Dong, L.; Shan, C.-X. One-step synthesis of multi-colored ZnO nanoparticles for white light-emitting diodes. *J. Lumin.* **2022**, *252*, 119425. [[CrossRef](#)]
39. Li, W.; Yang, H.; Jiang, X.; Liu, Q. Highly selective CO₂ adsorption of ZnO based N-doped reduced graphene oxide porous nanomaterial. *Appl. Surf. Sci.* **2016**, *360*, 143–147. [[CrossRef](#)]
40. Prerna; Agarwal, H.; Goyal, D. Photocatalytic degradation of textile dyes using phycosynthesised ZnO nanoparticles. *Inorg. Chem. Commun.* **2022**, *142*, 109676. [[CrossRef](#)]
41. Kusiak-Nejman, E.; Wojnarowicz, J.; Morawski, A.W.; Narkiewicz, U.; Sobczak, K.; Gierlotka, S.; Lojkowski, W. Size-dependent effects of ZnO nanoparticles on the photocatalytic degradation of phenol in a water solution. *Appl. Surf. Sci.* **2021**, *541*, 148416. [[CrossRef](#)]
42. Kuang, D.; Liu, L.; Mead, J.L.; Deng, L.; Luo, H.; Wang, S. Facile synthesis and excellent microwave absorption performance of ultra-small ZnO-doped onion-like carbon nanoparticles. *Mater. Res. Bull.* **2023**, *157*, 112007. [[CrossRef](#)]
43. Gnanasangeetha, D.; Thambavani, D.S. Biogenic production of zinc oxide nanoparticles using *Acalypha indica*. *J. Chem. Biol. Phys. Sci.* **2013**, *4*, 238.
44. Nasrollahzadeh, M.; Sajadi, S.M.; Rostami-Vartooni, A.; Hussin, S.M. Green synthesis of CuO nanoparticles using aqueous extract of *Thymus vulgaris* L. leaves and their catalytic performance for N-arylation of indoles and amines. *J. Colloid Interface Sci.* **2016**, *466*, 113–119. [[CrossRef](#)] [[PubMed](#)]
45. Vankudoth, S.; Dharavath, S.; Veera, S.; Maduru, N.; Chada, R.; Chirumamilla, P.; Gopu, C.; Taduri, S. Green synthesis, characterization, photoluminescence and biological studies of silver nanoparticles from the leaf extract of *Muntingia calabura*. *Biochem. Biophys. Res. Commun.* **2022**, *630*, 143–150. [[CrossRef](#)] [[PubMed](#)]
46. Momeni, S.S.; Nasrollahzadeh, M.; Rustaiyan, A. Green synthesis of the Cu/ZnO nanoparticles mediated by *Euphorbia prolifera* leaf extract and investigation of their catalytic activity. *J. Colloid Interface Sci.* **2016**, *472*, 173–179. [[CrossRef](#)] [[PubMed](#)]
47. Ojha, A.K.; Srivastava, M.; Kumar, S.; Hassanein, R.; Singh, J.; Singh, M.K.; Materny, A. Influence of crystal size on the electron–phonon coupling in ZnO nanocrystals investigated by Raman spectroscopy. *Vib. Spectrosc.* **2014**, *72*, 90–96. [[CrossRef](#)]
48. Procek, M.; Pustelny, T.; Stolarczyk, A. Influence of External Gaseous Environments on the Electrical Properties of ZnO Nanostructures Obtained by a Hydrothermal Method. *Nanomaterials* **2016**, *6*, 227. [[CrossRef](#)]
49. Arguello, C.; Rousseau, D.; Porto, S.; Cheesman, L.; Scott, J. Rayleigh scattering of linearly polarized light from optically active quartz. *Appl. Opt.* **1968**, *7*, 1913–1915. [[CrossRef](#)]
50. Mohamed, R.; Mkhali, I.; Baieissa, E.; Al-Rayyani, M. Photocatalytic degradation of methylene blue by Fe/ZnO/SiO₂ nanoparticles under visiblelight. *J. Nanotechnol.* **2012**, *2012*, 329082. [[CrossRef](#)]
51. Maness, P.-C.; Smolinski, S.; Blake, D.M.; Huang, Z.; Wolfrum, E.J.; Jacoby, W.A. Bactericidal activity of photocatalytic TiO₂ reaction: Toward an understanding of its killing mechanism. *Appl. Environ. Microbiol.* **1999**, *65*, 4094–4098. [[CrossRef](#)]
52. Hayat, K.; Gondal, M.A.; Khaled, M.M.; Ahmed, S. Kinetic study of laser-induced photocatalytic degradation of dye (alizarin yellow) from wastewater using nanostructured ZnO. *J. Environ. Sci. Health Part A* **2010**, *45*, 1413–1420. [[CrossRef](#)]

53. Irani, M.; Mohammadi, T.; Mohebbi, S. Photocatalytic Degradation of Methylene Blue with ZnO Nanoparticles; a Joint Experimental and Theoretical Study. *J. Mex. Chem. Soc.* **2016**, *60*, 218–225. [[CrossRef](#)]
54. Nosaka, Y.; Nosaka, A. Understanding Hydroxyl Radical ($\cdot\text{OH}$) Generation Processes in Photocatalysis. *ACS Energy Lett.* **2016**, *1*, 356–359. [[CrossRef](#)]
55. Ashokkumar, M.; Muthukumar, S. Electrical, dielectric, photoluminescence and magnetic properties of ZnO nanoparticles co-doped with Co and Cu. *J. Magn. Magn. Mater.* **2015**, *374*, 61–66. [[CrossRef](#)]
56. Mote, V.; Purushotham, Y.; Dole, B. Structural, morphological, physical and dielectric properties of Mn doped ZnO nanocrystals synthesized by sol-gel method. *Mater. Des.* **2016**, *96*, 99–105. [[CrossRef](#)]
57. Omar, K.; Ooi, M.J.; Hassin, M. Investigation on dielectric constant of zinc oxide. *Mod. Appl. Sci.* **2009**, *3*, 110. [[CrossRef](#)]
58. Gul, I.; Abbasi, A.; Amin, F.; Anis-ur-Rehman, M.; Maqsood, A. Structural, magnetic and electrical properties of $\text{Co}_{1-x}\text{Zn}_x\text{Fe}_2\text{O}_4$ synthesized by co-precipitation method. *J. Magn. Magn. Mater.* **2007**, *311*, 494–499. [[CrossRef](#)]
59. Sasi, S.; Fathima Fasma, P.H.; Bindu Sharmila, T.K.; Julie Chandra, C.S.; Antony, J.V.; Raman, V.; Nair, A.B.; Ramanathan, H.N. Green synthesis of ZnO nanoparticles with enhanced photocatalytic and antibacterial activity. *J. Alloys Compd.* **2022**, *924*, 166431. [[CrossRef](#)]
60. Liu, J.; Huang, J.; Hu, Z.; Li, G.; Hu, L.; Chen, X.; Hu, Y. Chitosan-based films with antioxidant of bamboo leaves and ZnO nanoparticles for application in active food packaging. *Int. J. Biol. Macromol.* **2021**, *189*, 363–369. [[CrossRef](#)]
61. Şahin, B.; Aydın, R.; Soylu, S.; Türkmen, M.; Kara, M.; Akkaya, A.; Çetin, H.; Ayyıldız, E. The effect of thymus syriacus plant extract on the main physical and antibacterial activities of ZnO nanoparticles synthesized by SILAR method. *Inorg. Chem. Commun.* **2022**, *135*, 109088. [[CrossRef](#)]
62. Naserian, F.; Mesgar, A.S. Development of antibacterial and superabsorbent wound composite sponges containing carboxymethyl cellulose/gelatin/Cu-doped ZnO nanoparticles. *Colloids Surf. B Biointerfaces* **2022**, *218*, 112729. [[CrossRef](#)]
63. Godoy-Gallardo, M.; Eckhard, U.; Delgado, L.M.; De Roo Puente, Y.J.; Hoyos-Nogués, M.; Gil, F.J.; Perez, R.A. Antibacterial approaches in tissue engineering using metal ions and nanoparticles: From mechanisms to applications. *Bioact. Mater.* **2021**, *6*, 4470–4490. [[CrossRef](#)]